Eur. Phys. J. D (2025)79:153
https://doi.org/10.1140/epjd/s10053-025-01102-x

THE EUROPEAN
PHYSICAL JOURNAL D

Regular Article - Plasmas

Impact of added capacitance and inductance on transient spark plasma characteristics and on HNO_2 generation

Mário Janda[a], Peter Tóth, and Sergei Smirnov

Faculty of Mathematics, Physics and Informatics, Comenius University in Bratislava, Bratislava, Slovakia

Received 23 September 2025 / Accepted 21 November 2025

Abstract. Electrical discharges offer a promising alternative for nitrogen fixation. This study investigates the properties of plasma generated by transient spark discharges in dry and humid air. Influence of an additional capacitor, both alone and combined with an inductor on the transient spark's electrical and optical characteristics is examined. The study also describes the influence of the circuit configuration on HNO_2 generation in humid air and in a humid N_2/NO (2000 ppm) mixture.

With both a capacitor and an inductor in the driving circuit, the plasma sustains for 4–5 µs after the initial spark pulse, exhibiting several "re-ignitions." Electrons probably gain relatively high energy during these "re-ignitions," as they are capable of exciting N_2 to energy levels exceeding 11 eV. Concurrently, the electron density remains above approximately 10^{21} m^{-3} for several microseconds. The enhanced efficiency in NO formation in driving circuit with both capacitor and an inductor is most likely due to a substantial increase in the heavy particle temperature, reaching 5000–7000 K, during this discharge phase. However, these prolonged, high-temperature conditions are likely detrimental to HNO_2 formation, which is more efficiently generated in driving circuits without additional inductor.

1 Introduction

Fertilizers are essential for boosting crop yields and ensuring sufficient food production for the world's growing population [1]. Currently, the majority of fertilizers rely on ammonia (NH_3) as their primary source of nitrogen, predominantly produced through the Haber–Bosch process [2]. The Haber–Bosch process combines nitrogen from the atmosphere with hydrogen under high pressure and temperature to synthesize ammonia. Besides high pressure and temperature, presence of catalysts is needed [3]. While crucial for food production, the Haber–Bosch process is energy-intensive and relies on fossil fuels, contributing to greenhouse gas emissions [4, 5].

The widespread use of ammonia-based fertilizer thus raises significant environmental concerns [6]. Consequently, scientists are actively researching and developing alternative fertilizer types that aim to be more sustainable. These efforts encompass exploring more efficient nitrogen utilization by plants [7, 8], improving fertilizer delivery methods [9], developing bio-based fertilizers [10], or other nitrogen fixation method to replace Haber–Bosch process [11, 12].

Plasmas also offer a promising alternative for nitrogen fixation, encompassing both thermal and non-thermal approaches [13–17], either by production of NH_3 [14, 18], or by production of nitrogen oxides [19–21]. A disadvantage of plasma-based methods is a significant amount of energy input to generate and sustain the plasma. While theoretically some plasma methods have the potential for higher energy efficiency [22], currently, the Haber–Bosch process, despite its high-pressure needs, often achieves better overall energy efficiency in practice, especially at large scales [23].

A significant advantage of plasma-based nitrogen fixation over the Haber–Bosch process is the ease of turning plasma systems on and off provides operational flexibility and responsiveness to fluctuating demands. Furthermore, many plasma methods can operate in atmospheric pressure using air as a direct input for producing nitrogen oxides (NOx). Using air as only input chemical can be considered as another important advantage compared to Haber–Bosch process.

Supplementary Information The online version contains supplementary material available at https://doi.org/10.1140/epjd/s10053-025-01102-x.

[a] e-mail: janda@fmph.uniba.sk (corresponding author)

Several types of electrical discharges can efficiently generate NOx in air. Dielectric barrier discharges (DBDs) operating at higher power levels are one such method [24]. Microwave discharges offer another route to NOx production [19, 23]. Gliding arc discharges, characterized by a long, diffuse arc, can also generate these species [21]. Transient spark discharges, which are short-lived and high-energy, represent a further source of NO and NO_2 [20, 25]. Another reactive nitrogen species (RNS) generated by non-thermal plasmas include nitrous oxide (N_2O) or dinitrogen pentoxide (N_2O_5) [26–28]. In the presence of humidity, OH radicals are generated in plasma and nitrogen oxides can be converted to nitrous and nitric acids [29, 30].

The formation of gaseous RNS is only the first step. For a successful nitrogen fixation process, these RNS must be trapped. Post-discharge trapping of reactive nitrogen species from plasma into water offers a viable approach for nitrogen fixation [31]. An alternative strategy involves directly generating the plasma in contact with water. This direct interaction leads to the formation of what is known as plasma-activated water (PAW) [32, 33], with potential applications in agriculture, medicine, and food processing [34–36].

The specific composition of PAW depends on the type of discharge, reactor configuration, discharge polarity or power [37–39]. Further research is needed to optimize the production of PAW with desired properties and with improved energy efficiency. The initial step being more efficient production of gaseous RNS, especially those highly soluble in the water, such as HNO_2 [30], N_2O_5 or HNO_3 [40].

Generation of HNO_2 in humid air by transient spark (TS) discharges was shown to significantly enhance NO_2^- formation in PAW [30]. TS are DC driven self-pulsing discharges that produce short (approximately 10–100 ns) spark current pulses with typical repetition frequencies of 1–10 kHz [41, 42]. Without additional external capacitor in the circuit, these pulses are formed only thanks to the internal capacitance of TS driving circuit.

In our recent paper, we examined the effect of adding a capacitor and inductor to the driving circuit of transient spark discharges in dry air, where dominant gas phase products are NO and NO_2 [25]. We demonstrated a positive effect of an additional inductor on the efficiency of NO generation. This paper further investigates transient spark discharges with added capacitor and inductor using time-resolved optical emission spectroscopy. Simultaneously, electrical measurements were performed with better resolution, both in dry and humidified air. The primary goal is to understand the enhanced NO generation by analyzing the time evolution of electron density and gas temperature. In addition, experiments were performed in humid N_2/NO mixture to study influence of the circuit characteristics on HNO_2 production. Obtained results provide insights for further optimization of nitrogen fixation by TS discharges.

2 Method

Figure 1 shows a simplified schematic of the experimental setup, which comprises several components. First, the electrical circuit and a reactor (Sect. 2.1) generate a transient spark discharge. Dry synthetic air (80% N_2, 20% O_2, 99.99% purity), controlled at 1.0 L/min by a mass flow controller (Bronkhorst FLEXI-FLOW), serves as the inlet gas. For some experiments, the air is humidified by bubbling it through deionized (DI) water before entering the reactor, typically achieving a relative humidity of 94–96%, as verified by a capacitive humidity sensor (Arduino DHT-11). The light emitted by the discharge is analyzed by optical diagnostic techniques described in Sect. 2.2.

One set of experiments was performed in a humidified mixture of NO (2000 ppm) in N_2 (Linde Gas). The analytical technique used to determine HNO_2 concentration after the treatment was UV–Visible absorption spectroscopy. A deuterium lamp (Avantes AvaLight-D-S) was used as the light source and absorption spectra were measured with an optical emission spectrometer (Avantes AvaSpec-Mini4096CL). The spectral resolution of this system is 0.5–0.7 nm and spectra in the range 190–650 nm were recorded. More details can be found in Ref. [25].

2.1 Driving circuit and reactor

The discharge was generated by a DC high-voltage (HV) power supply (Technix RS20) connected to the anode via a series resistor, R, ranging from 3 to 10 MΩ. The anode was a flat stainless steel needle with an outer diameter of 0.7 mm. The grounded cathode was a steel M6 screw with a rounded end. The distance between the electrodes was 8 mm. Despite using a DC power supply, the electrical circuit shown in Fig. 1 generates a self-pulsing 'transient spark' discharge. In the simplest configuration, the discharging capacitance is

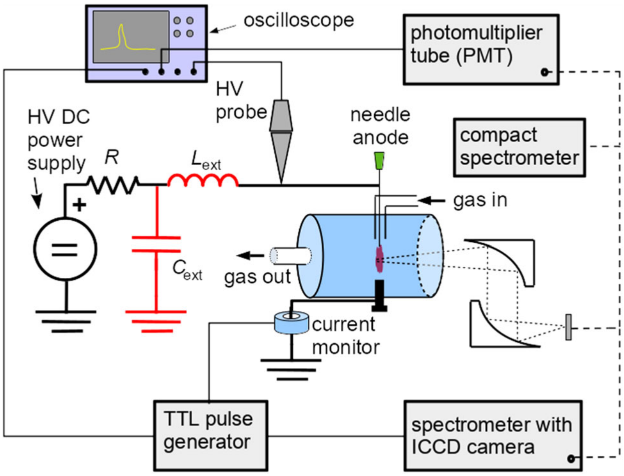

Fig. 1 Simplified schematic of the experimental setup

provided only by the internal capacitance of the circuit (C_{int} ˜ 25 pF).

In this work, we study the effect of additional circuit components—the external capacitor, C_{ext} (50 pF), and the inductor, L_{ext} (0.73 mH)—on the transient spark discharge properties. These components, C_{ext} and L_{ext}, are optional and are shown in red in Fig. 1. The transient spark circuit with an added external capacitor is labeled TS-C, and the circuit with both an external capacitor and an inductor is labeled TS-LC. The original transient spark circuit without additional capacitor or inductor is labeled TS.

Electrical discharge characteristics were measured using a HV probe (North Star PVM-12) and a current probe (Hioki 3273-50) connected to a digital oscilloscope (Rigol DHO924S, 250 MHz, 12-bit ADC, 1.25 GSa/S). The recorded waveforms were used to calculate the discharge power and specific input energy SIE [J/L], as described in Ref. [43]. In the majority of experiments presented in this paper, we aimed to maintain the same SIE around 300 J/L, with an uncertainty of up to 25%, when comparing different TS driving circuits. Only in experiments focused on HNO_2 generation in the humid N_2/NO mixture was the SIE varied. This was done to obtain the dependence of HNO_2 concentration on the SIE and on the total power delivered by the power supply. The total power was calculated from the mean current and mean voltage at the power supply's output.

2.2 Optical diagnostic method

A two-channel compact emission spectrometer (Ocean Optics SD2000) with a 200–1100 nm range and a resolution of 0.6–1.2 nm was used to record time-integrated spectra. Time-resolved measurements of the emission intensity were made with a photomultiplier tube (PMT) with a rise time of 2.2 ns (Hamamatsu H955). The time evolution of specific spectral ranges can be measured with the PMT by inserting bandpass interference filters into the optical path. The PMT module signal was recorded using an oscilloscope.

The time-resolved emission spectra were obtained using an iCCD camera (Andor iStar) with a time resolution as low as 2 ns, coupled to a 2 m spectrometer (Carl Zeiss Jena PGS2). The spectrometer has a resolving power of 45,000, covering the UV and VIS regions (200–800 nm). The full width at half maximum (FWHM) of the instrumental broadening, measured by a He–Ne laser, changes between 0.04 and 0.09 nm for entrance slit widths of 30 μm and 100 μm, respectively. Below 30 μm, the entrance slit cannot further improve the spectral resolution, due to limitations imposed by the size of the CCD chip pixels.

The iCCD camera was triggered by a 5 V rectangular pulse generator, triggered directly by the rising slope of the discharge current signal. With a 2 m long optical cable, we were unable to acquire the initial 25 ns of the emission due to a delay caused by the trigger generator, the signal transmission time in BNC cables, and a camera gate delay. Therefore, we also made measurements using a 10 m long optical cable (Ocean Optics P400-10-UV–VIS). Here, the delay between the current signal and the camera gate opening was compensated, and it was possible to observe the initial emission phase of the transient spark.

The same iCCD camera was used for time-resolved TS spark channels imaging, with the spectrometer set to 0th order, and fully opened entrance slit (300 μm). During the imaging, optical fibers were not used and we could not observe initial ˜ 35 ns of the spark evolution.

The relatively fine spectral resolution of our spectrometer enables us to observe the broadening of atomic and ionic lines caused by free electrons in the plasma, a phenomenon known as the Stark effect [44, 45]. The measurement of this emission lines' Stark broadening is the most common OES method for calculating the electron density (n_e) in atmospheric pressure plasmas. Here, the electron density was calculated by several methods. First, we estimated n_e from the full width at half area (FWHA) of the Hα, using the formula derived by Gigosos et al. [46]:

$$\Delta\lambda_A = 0.549 \times \left(\frac{n_e}{10^{23}}\right)^{0.67965}. \tag{1}$$

Here, $\Delta\lambda_A$ is the FWHA of the Hα line in nm, and n_e is in m^{-3}. This formula is valid for electron densities between 10^{20} and 10^{25} m^{-3} and for electron temperatures between 1 and 175 kK [46]. Next, we estimated n_e from the FWHM of the Hα line, $\Delta\lambda_{1/2}$, using the formula:

$$\Delta\lambda_{1/2} = 2.8 \times 10^{-17} n_e^{0.72}. \tag{2}$$

This formula is useful for n_e ranging from 10^{23} to 10^{25} m^{-3}. In this range of electron densities, the dependence of the Stark broadening of this line on the electron temperature is negligible [47]. The Hα line profile was fitted to separate the influence of the collisional broadening from the instrumental broadening, Doppler effect, and a natural line width. The collisional broadening could be caused by both the Stark effect and van der Waals broadening. However, at the high temperatures achieved in the spark plasma channel, we estimated that the van der Waals broadening effect is negligible.

Finally, we estimated n_e by comparing experimental spectra of the O triplet line near 777 nm with spectra simulated using the Specair software [48, 49]. Besides the Stark effect, the spectra calculated by Specair take into account the natural line width, Doppler effect, van der Waals broadening, and instrumental broadening. A disadvantage is the dependence of the Stark effect on the electron temperature. We therefore calculated spectra for electronic excitation temperature from 10 to 40 kK. The advantage of using the O triplet line is its weaker broadening compared to the Hα line. O triplet line could be used for n_e estimation in the initial spark phase, when the Hα line was so broadened that we could

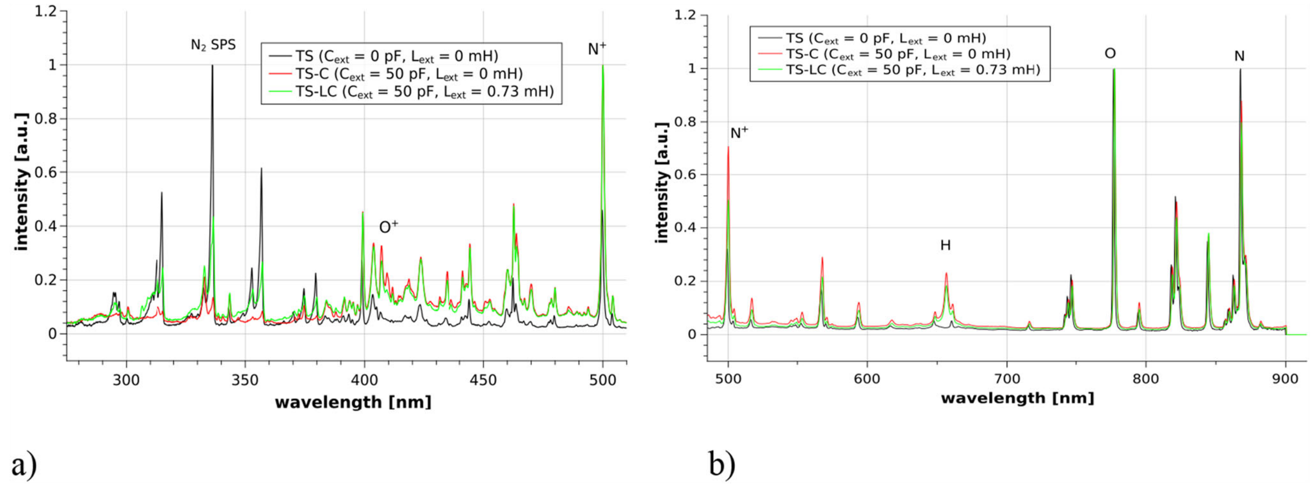

Fig. 2 Normalized, time integrated, optical emission spectra of transient spark discharges in humidified air, with driving circuit containing $C_{\mathrm{ext}} = 50$ pF and $L_{\mathrm{ext}} = 0.73$ mH

not capture the entire line profile with our spectrometer.

Several other plasma characteristics can be obtained by the OES technique, for example a rotational, or electronic excitation temperatures of some species in the plasma [50, 51]. The rotational temperature of $N_2(C^3\Pi_u)$, often used to approximate gas kinetic temperature, can be obtained by fitting the experimental spectra of the molecular nitrogen second positive emission system (SPS), which corresponds to the transition from the $N_2(C^3\Pi_u)$ state to the $N_2(B^3\Sigma_g)$ state. For this purpose, we used synthetic spectra generated by the Specair software [48, 49].

With the combination of C_{ext} and L_{ext} in the circuit, the amplitude of the TS-LC initial pulse is comparable to the amplitude of a basic TS discharge current peak. The additional inductor L_{ext}, however, increases the length of the discharge active phase up to ˜ 4 to 5 μs. During this period, the current oscillations in the circuit with L_{ext} are not simple damped sinusoidal oscillations (Figure S2 in Supplementary material), but the voltage and current oscillations are influenced by the low resistance of the plasma channel. Several plasma 're-ignitions' can be observed during this period, accompanied by an increase of the emission intensity, as shown in the next section.

3 Results and discussion

3.1 Electrical characteristics

In this investigation, the influence of an additional capacitor and inductor on electrical characteristics and transient spark discharge waveforms were studied using dry air, humid air and a humid N_2/NO mixture. Notably, the presence of humidity did not yield any significant difference when compared to the results obtained in dry air, described in details in our recent publication [25].

In summary, the amplitude of the TS-C current pulses (with additional C_{ext} but without L_{ext}) is higher compared to the basic TS discharge, which has no additional capacitor (Fig. S1 in Supplementary material). Furthermore, the subsequent current oscillations following the initial current peak become more pronounced and prolonged using C_{ext}. The observed damped oscillations are attributed to RLC oscillations, where C represents the total circuit capacitance, L is the intrinsic inductance of the circuit, and R is the plasma resistance.

3.2 Plasma emission characteristics

Figure 2a shows three normalized time-integrated emission spectra in the range of 275–510 nm, generated using different driving circuits: no external capacitor or inductor (TS), additional capacitor only (TS-C), and both additional capacitor and inductor (TS-LC). The strongest emission line in the spectra of TS-C and TS-LC is the N^+ ion line near 500 nm. This N^+ line is also prominent in the emission spectrum of the TS discharge without additional capacitor and inductor. However, in TS, the emission from the N_2 second positive system (270–370 nm) dominates the spectra.

In our previous work, we observed that the emission of molecular nitrogen is generated mainly during the pre-breakdown streamer phase of the transient spark [42, 52]. Thus, the observed variation in the relative N_2 SPS intensity shown in Fig. 2a could be explained by a higher emission intensity during the spark phase compared to the streamer phase in transient sparks generated with an additional inductor and capacitor, or with a capacitor only. This is consistent with the higher energy per pulse in these cases.

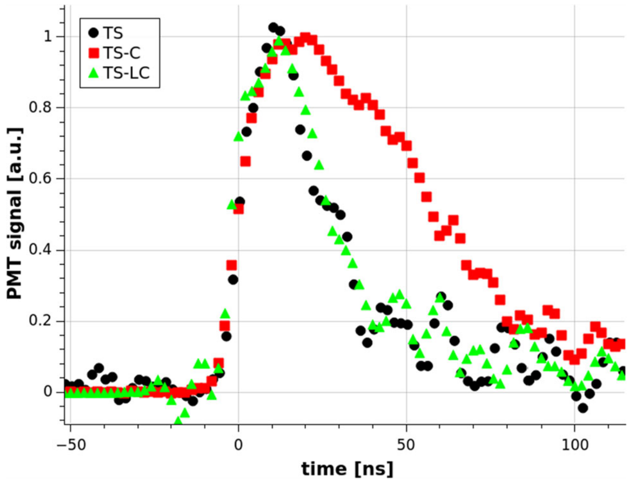

Fig. 3 Inverted PMT signal measured with bandpass interference filter with central wavelength 500 nm, FWHM 10 nm, different TS driving circuits, averaged over 128 pulses

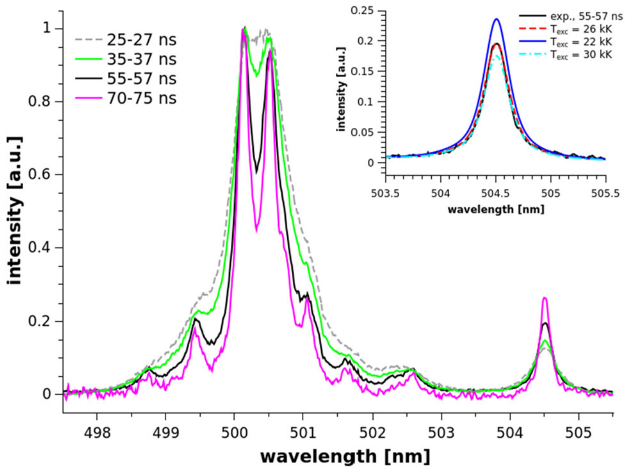

Fig. 4 Time evolution of normalized emission spectra of N^+ lines in the range 495–505 nm, transient spark discharge with additional capacitor (TS-C). Inlet figure: fitting of line at 504.5 nm (time 55–57 ns after the beginning of the spark) by synthetic spectra with different T_{exc}

The emission spectra in Fig. 2a show that, in addition to the emissions from N^+ near 500 nm and N_2 SPS mentioned above, there are multiple emission lines between 375 and 490 nm from O^+ and N^+, as well as bands from the first negative system (FNS) of $N_2{}^+$. The O^+ and N^+ lines are also visible in the spectra in Fig. 2b, at wavelengths below 660 nm. At longer wavelengths, various emission lines of neutral O and N atoms are present, with the O line near 777 nm having the highest intensity. Interestingly, adding capacitor and inductor to TS driving circuit significantly increased intensity of Hα emission line near 656 nm, but the OH(A–X) emission system around 300–310 nm remained very weak compared to N_2 SPS.

Based on the spectra shown in Fig. 2a and b, suitable lines and emission systems for time-resolved spectroscopic studies were selected: the N^+ line near 500 nm, the N_2 SPS band near 337 nm (0–0 vibrational transition), the O triplet line near 777 nm, and the Hα line near 656 nm for calculating electron density from its Stark broadening. Using a PMT, we studied either the total emission intensity evolution or the evolution of the N^+ line near 500 nm and the O line near 777 nm. The N_2 SPS 0–0 band and Hα line were not studied by PMT because the interference bandpass filters used were not able to separate emissions from nearby N^+ ionic emission lines.

Figure 3 illustrates the normalized light emission evolution of the N^+ line near 500 nm, measured by a photomultiplier with an interference filter, following the current pulse. The emission profiles obtained using different driving circuits for transient spark generation are compared. It is notable that the N^+ emission evolution for TS and TS-LC is nearly identical. This can be attributed to the similar amplitude of their initial current pulses (Fig. S1) and the approximately equivalent amount of energy delivered to the gap during this initial pulse. Although TS-LC exhibits secondary current pulses, delivering additional energy to the gap over the subsequent 4–5 μs, this does not result in the production of excited N^+ ions.

Conversely, the duration of N^+ emission is extended solely in the case of TS-C, where additional capacitor, but no additional inductor, is present in the circuit. This suggests a higher degree of ionization and atomization achieved in the TS-C discharge compared to the standard TS discharge. The electrical characteristics of TS-C corroborate this observation: its current pulses have a higher amplitude (Fig. S1), and a significantly larger amount of energy is delivered to the gap during the gas breakdown phase, as compared to TS.

Altogether, even in the case of TS-C, the PMT measurements with a 500 nm filter show a short lifetime of ionic species, such as N^+. However, measurements with an interference filter for 780 nm, specifically selecting the O triplet line near 777 nm, show that the emission of neutral atomic lines reaches its peak value shortly after the N^+ lines (with a delay of about 25 ns), and their lifetime is longer. In the case of TS-LC, the emission of atomic oxygen reappears during the secondary discharge re-ignitions. These results were also confirmed by time-resolved spectra measured by a high-resolution spectrometer coupled with an iCCD camera.

Figure 4 shows normalized time-resolved emission spectra of several N^+ lines in the range 495–505 nm observed in plasma generated by a transient spark discharge with an additional capacitance of 50 pF, TS-C. Figure 4 illustrates a significant line broadening effect, which becomes less prominent with increasing time relative to the beginning of the spark pulse. This broadening mechanism can be dominantly attributed to the Stark effect caused by the high density of free electrons. However, we did not use the N^+ line spectra to calculate the electron density. As discussed later, we used the Hα line for this purpose.

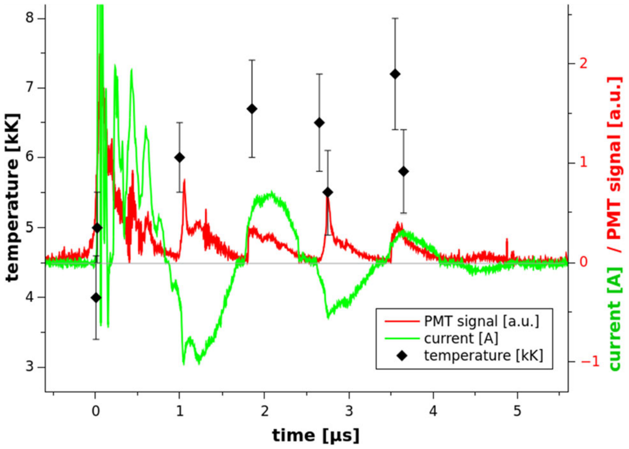

Fig. 5 Inverted PMT signal measured without bandpass interference filter (red line), single discharge event current waveform (green line), and temperature estimated from N_2 SPS emission spectra (black points), transient spark with additional capacitor and inductor (TS-LC)

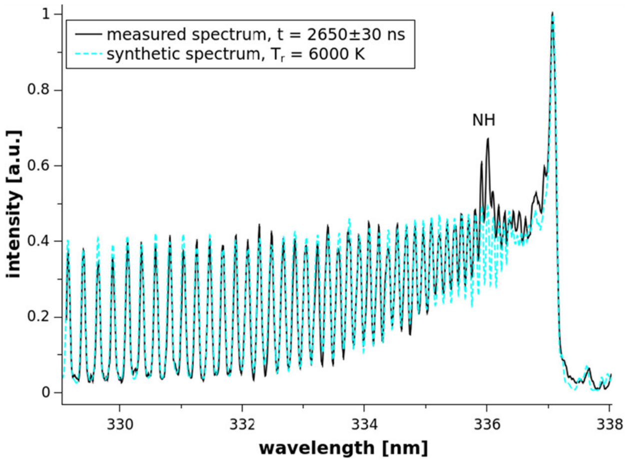

Fig. 6 Normalized time-resolved emission spectrum of N_2 SPS 0–0 band, time 2650 ± 30 ns after the beginning of TS-LC spark current pulse, comparison with normalized synthetic spectrum calculated for rotational temperature of 6000 K

Concerning the spectra of N^+ lines, we focused here on the electronic excitation temperature of N^+ ions, T_{exc}. This can be estimated by comparing the relative intensity of the line at 504.5 nm to the intensity of the group of lines around 500.5 nm. It was found that in TS-C, where the N^+ line intensity is strong enough to be fitted for about 100 ns after the beginning of the spark pulse, the N^+ excitation temperature decreased from around 30 kK down to 25 kK. In spectra from TS and TS-LC, the emission intensity of N^+ lines dropped too low after about 50 ns, so no trend in the T_{exc} evolution was observed; it remained at approximately 25 kK.

Although the N^+ emission duration was longest in TS-C, the total emission was significantly longer in TS-LC. Figure 5 displays the total emission intensity profile from a single discharge event, measured by PMT and aligned with the current waveform. The initial current pulse peak has been cut-off to focus on the subsequent current evolution. In the TS-LC discharge, emission was observed for nearly 5 µs after the initial breakdown. However, the emission intensity was not constant; secondary peaks appeared, corresponding to increases in the discharge current. We refer to these events as discharge re-ignitions.

As previously mentioned, no significant emission from ionic lines was observed during these re-ignitions. However, there was emission from atomic lines and, more notably, strong emission from the second positive system of N_2. This emission system was utilized to estimate the rotational temperature (T_r) of the $N_2(C^3\Pi_u)$ state, which is commonly considered a good approximation of the gas kinetic temperature in air plasmas [50]. For this purpose, the experimental spectra were fitted using the Specair software [48, 49]. Figure 6 presents a representative, normalized, time-resolved emission spectrum of the N_2 SPS (0,0) band, with the emission collected at 2650 ± 30 ns after the beginning of the TS-LC spark current pulse. The experimental spectrum is compared with a synthetic spectrum calculated for a T_r of 6000 K. For each time interval, at least four spectra were recorded, each being an accumulation over 100 TS-LC pulses.

Figure 5 displays the time evolution of T_r. Despite a relatively high degree of uncertainty, the rotational temperature clearly reaches high values. Based on our previous results [42], the temperature in the plasma channel of a transient spark increases to approximately 1000 K shortly before breakdown. This indicates that during the initial spark current pulse, the temperature rises rapidly to about 4000 K within 50 ns. Subsequently, during the secondary pulses in the TS-LC discharge, it continues to increase at a slower rate, reaching up to approximately 7000 K.

It is generally believed that $N_2(C^3\Pi_u)$ excited states are primarily generated by the direct electron impact excitation of ground-state molecular nitrogen [53]. However, this process only occurs when the reduced electric field is sufficiently strong (> 80 Td), ensuring the presence of enough high-energy electrons to overcome the high energy threshold (> 11 eV) for this excitation. In a transient spark with no additional inductor in the driving circuit, the N_2 SPS emission is mainly generated during the pre-breakdown streamer phase and the initial phase of the spark current pulse while the current is still increasing. Subsequently, the N_2 SPS emission disappears due to the voltage drop and the resulting weak electric field.

The reappearance of N_2 SPS emission in later re-ignition phases of TS-LC indicates a significant increase in electron mean energy, due to the high energy threshold for $N_2(C)$ excitation. This also implies a relatively strong reduced electric field strength in these later phases of TS-LC. Based on the measured voltage waveforms (Fig. S2), the discharge voltage does only reach approximately 600 V (in absolute value). However, if we consider a temperature elevated to about 6000 K,

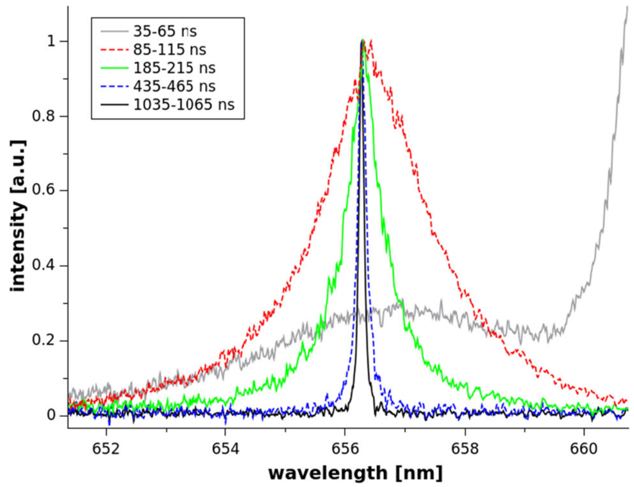

Fig. 7 Normalized time-resolved emission spectra of Hα line; TS-LC; measured at different time windows after the beginning of the spark current pulse

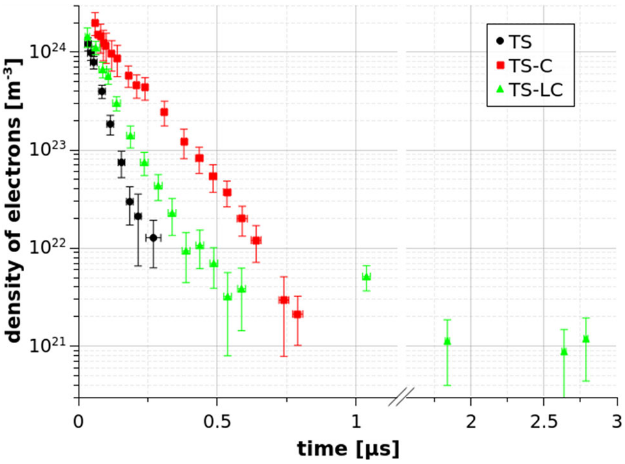

Fig. 8 Time evolution of estimated electron density after the spark pulse, different transient spark driving circuits, estimated from FWHA of the Hα line

assuming a pressure close to 1 atm, the density of neutral species is approximately 20 times lower than at 300 K. Consequently, with 600 V and 6000 K, the average reduced field strength should be comparable to that at 300 K and 12 kV.

Besides electron energy, their concentration is also crucial in terms of plasma chemistry. For all three investigated discharge variants, we monitored the evolution of electron density based on the broadening of the Hα emission line (Fig. 7). Figure 8 illustrates the time evolution of electron density estimated from the FWHA of the Hα line (Eq. 1). This comparison focuses on three different electrical circuit configurations that generate plasma, TS-C, TS-LC, and TS.

Figure 8 shows that the rate of electron density decay over time differs for each circuit configuration. The slowest decay was observed in the TS-C configuration, while the fastest decay occurred in the TS configuration. This observation correlates with the duration of the current pulse—a longer current pulse in TS-C leads to a slower decrease in electron density. In the case of TS-LC, the initial rate of electron density decay falls between TS-C and TS. Although the primary current pulse in TS-LC is roughly the same as in TS, the electron density here decreases more slowly, likely due to the relatively rapid appearance of additional, secondary pulses caused by the added inductor. These secondary pulses seemingly play a crucial role in slowing down the electron density decay compared to TS. Thanks to them, TS-LC maintains a relatively high electron density, at a level of 10^{21} m^{-3}, even approximately 3 μs after the initial pulse. This is significantly longer than what is measurable in the TS-C configuration, suggesting a more prolonged plasma with relevant electron density in TS-LC.

Another reason for the slow decrease in electron density in TS-LC could be the high gas temperature, estimated to be between 5000 and 7000 K. At such temperatures, the conversion of electrons to negative ions can likely be neglected. Furthermore, higher molecular ions, such as O_4^+ and N_4^+, are not stable under these conditions, and the recombination rate of electrons with N_2^+ and O_2^+ ions is significantly slower.

Concerning the peak electron density indicate that TS-C and TS-LC achieve similar maximum electron densities (Fig. 8). In contrast, the basic TS configuration exhibits a lower maximum n_e, approximately half that of TS-C and TS-LC. Nevertheless, this still represents a high density, reaching approximately 10^{24} m^{-3}.

We used n_e calculation method based on FWHA for comparison of discharges generated by three different driving circuit configurations due to its independence from electron temperature and the broad range of densities over which it is applicable. While it certainly compares the trends in the electron density evolution between the three circuits well, the maximum electron density in the initial spark phase is almost certainly overestimated. The gas density at atmospheric pressure and a temperature of 4000 K would be approximately 2×10^{24} m^{-3}. In the TS-C configuration, the obtained electron density would indicate a degree of ionization close to 1. We therefore verified the electron density using other methods, specifically by estimating it from FWHM of the Hα line (using Eq. 2) and by fitting the O triplet line at 777 nm.

Figure 9 compares electron density estimated by three different methods. For fitting of O triplet line, two different electronic excitation temperatures are shown, 10 kK and 40 kK. Figure 9 shows only initial 500 ns, because the O line is not broadened enough in the later phase. On the other hand, thanks to weaker broadening, we see the whole triplet line even in the very early phase of the spark when Hα line is significantly broadened and partly covered by a N^+ line near 661 nm. The estimate of electron density from FWHM of Hα line is shown only for n_e above 10^{23} m^{-3}, where Eq. 2 should be valid.

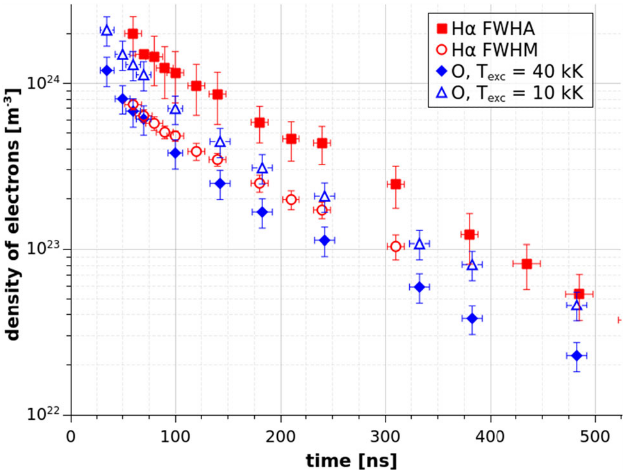

Fig. 9 Time evolution of estimated electron density after the spark pulse, TS-C, comparison of different calculation methods

Figure 9 shows that n_e estimated from FWHM of the Hα line is significantly lower as value obtained from FWHA of Hα line. In the initial spark phase, n_e from FWHM of the Hα line is similar to values obtained by O line fitting for electronic temperature of 40 kK. Later, the n_e calculated from the FWHM of the Hα line approaches the value obtained by O line fitting for the electronic temperature of 10 kK. This could indicate drop of electron temperature during the spark evolution.

The peak electron density calculated from the FWHM of the Hα line is still very high, around 7×10^{23} m^{-3}. It is possible that this value is still overestimated. There are several possible explanations.

First, an externally applied electric field (F_c), which is still strong at the beginning of the spark, also induces the Stark effect. Bastien and Marode [54] showed how the line profile may change with the parameter with the electron temperature T_e, and a $p_c = F_c/F_0$, where F_0 is a Holtsmark field, i.e., the electric microfield that an excited atom experiences due to the random, chaotic motion and distribution of nearby charged ions. Referring to [54], we showed that the influence of F_c on Stark broadening during the initial phase should be minor but not negligible in TS without additional capacitor and inductor [55]. In TS-C and TS-LC, however, the initial density of electrons and ions is higher than in TS. Resulting F_0 must be stronger, and the parameter p_c smaller, with even less significant influence of F_c on the Stark broadening of Hα line.

Next, we must take into account the radial distribution of all gas and plasma parameters during the spark channel evolution [56]. The spark current pulse is accompanied by a shock-wave formation. While the density of heavy particles in the core of the plasma channel decreases, the core is surrounded by a shock wave where the pressure can reach 2.5 bar [56]. The photons generated in the plasma core could be absorbed in this high-density zone, influencing the shape and width of the emission lines. A recent theoretical model shows that even non-resonance lines, such as the O triplet at 777 nm, could be influenced by this absorption at higher temperatures and increased atomic oxygen concentration [57]. This could probably also happen to the Hα line.

Concerning the above-mentioned strong radial dependence of gas and plasma parameters in the spark channel, we must note that the electron density we measured may be higher than the average value within the plasma channel. To calculate the average electron density, we would need to measure the radial distribution of n_e. This typically requires laterally scanning the spark plasma channel, followed by an Abel inversion—however, our measurement is currently limited to a line-of-sight (LoS) observation. It is therefore plausible that a significant portion of the photons detected from excited H atoms originates from the core of the plasma channel, where the electron density is higher than the average value.

Unfortunately, it is not feasible to perform a lateral scan of the TS channel. The diameter of an individual TS-C spark channel is approximately 55 ± 10 µm, while the diameter of the optical fiber's core used in our experiments is 400 µm. Even if a thinner optical fiber was employed, the obtained radial distribution would be primarily determined by the positional probability of the transient spark plasma channels appearing at a given distance from the inter-electrode axis. This is because when accumulating over many pulses, the individual spark channels change their position with respect to the LoS with each pulse (Fig. S3 in the Supplementary Material).

The diameter of the TS-C channel, mentioned above as 55 ± 10 µm, was estimated from time-resolved photographs of single spark channels taken at a delay of 35 ns from the beginning of the spark current pulse, using an exposure time of 5 ns. For a more accurate approximation of the plasma diameter, a FWHM of the spectrally unresolved radial intensity profile of the plasma channel was used. Summing the intensity profiles from several rows on the iCCD chip was used to improve signal-to-noise ratio.

We also captured images of TS and TS-LC plasma channels and attempted to measure the time evolution of the plasma diameter for all three circuit configurations. The major difference was the much weaker emission intensity of the TS and TS-LC channels compared to TS-C. Therefore, we were only able to follow the TS channel evolution for the initial ˜60 ns, compared to 300 ns in TS-C. We observed no statistically significant variation in the plasma diameter for either TS or TS-C within these time scales. In the case of TS-LC, we were able to capture single channel with a sufficiently strong signal for the initial 200 ns and then later during the moments of plasma re-ignitions. With delays above 1 µs, the plasma diameter increased slightly over time and almost doubled 2 µs after the beginning of the spark channel.

With respect to the plasma diameter of transient spark plasma channels, it is interesting to note that

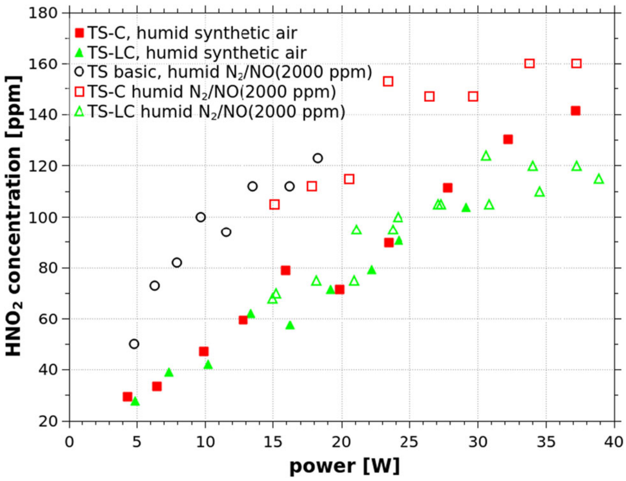

Fig. 10 Dependence of HNO_2 concentration on HV generator output power, produced by TS, TS-C and TS-LC discharges in humid air and humid N_2/NO mixture

while the average specific input energy is relatively low, around 300 J/L, the energy density within the plasma channel itself is much higher, on the order of 10^5 J/L. The reason for this discrepancy is that, in transient spark discharges, the majority of the gas is not converted into the highly conductive plasma with a high degree of atomization. However, the surrounding is involved in the chemistry induced by TS indirectly, thanks to the fast and efficient turbulent mixing that follows the shock wave caused by the spark.

3.3 HNO_2 formation

Figure 10 shows dependence of HNO_2 concentration on HV generator output power, produced by TS, TS-C and TS-LC discharges in humid air and humid N_2/NO mixture. The formation of HNO_2 in these transient spark discharges likely proceeds via the three-body reaction:

$$NO + OH + M \rightarrow HNO_2 + M. \qquad (3)$$

The HNO_2 production rate is thus dependent on the product of the NO and OH concentrations. It has been previously shown that the TS-LC circuit generates a higher concentration of NO at the same SIE compared to the TS and TS-C configurations [25]. Therefore, if the amount of OH radicals generated is similar across all transient spark discharges, the TS-LC discharge should produce HNO_2 in humid air more efficiently than the TS-C discharge.

Interestingly, Fig. 10 shows that the additional inductor in the circuit has no positive effect on the HNO_2 generation. Although the TS-C discharge produces less NO than the TS-LC discharge, it generates HNO_2 just as efficiently. This result suggests that, in humid air, the NO concentration generated by the discharge is not the rate-limiting factor for HNO_2 formation.

To eliminate the NO generation advantage of the TS-LC configuration and isolate the influence of the OH radical concentration, the experiments in a gas mixture of N_2 with 2000 ppm of NO were performed. The mixture was humidified by passing it through deionized water in a bubbler.

The concentration of HNO_2 produced by the TS-LC discharge in the humid N_2/NO mixture remained unchanged compared to the experiment in humid air. This observation confirms that the NO concentration is not the limiting factor for HNO_2 formation by the TS-LC discharge. Conversely, in the TS-C discharge, the HNO_2 production efficiency increased significantly in the humid N_2/NO mixture compared to humid air. Consequently, the TS-C discharge generates HNO_2 more efficiently than the TS-LC discharge when operating in the N_2/NO mixture. This superior performance suggests a more efficient generation of OH radicals by the stronger TS-C pulses. To definitively prove this hypothesis, in situ measurements of OH radical formation, for example using the Laser-Induced Fluorescence (LIF) technique, would be necessary.

In the basic TS configuration, without additional circuit components, the initial HNO_2 concentration is very small, possibly due to a low amount of produced OH radicals. As the power increases, the TS discharge produces HNO_2 with the same efficiency as TS-C. Among the three variants studied, the TS-LC circuit appears to be the least suitable for HNO_2 formation.

There is one additional possible explanation for this besides the potentially less efficient formation of OH radicals. Based on our previous findings, we hypothesize that the enhanced NO production in TS-LC is attributable to the prolonged duration of the plasma characterized by high gas temperature and a relatively high electron density of approximately 10^{21} m^{-3}. However, these prolonged, high-temperature conditions are likely detrimental to HNO_2 formation. This more complex molecule is less stable at such high temperatures, and the rate of the three-body reaction (3) also decreases if the density of the collision partner M is reduced.

In the TS-C and TS discharges, the plasma channel duration is significantly shorter than in TS-LC. The resulting fast and efficient turbulent mixing of the plasma channel, which contains the NO and OH radicals, with the surrounding cold gas is likely highly beneficial for the subsequent HNO_2 formation.

4 Conclusions

This research focuses on characterizing plasma generated by a self-pulsing electrical discharge, known as a transient spark, in dry air. We investigated the influence of adding a capacitor (50 pF) alone and a capacitor combined with an inductor (0.73 mH) on the electrical and optical properties of the transient spark. Our primary goal was to explain the increased efficiency of NO formation when an inductor is added to the transient spark generation circuit. Next, we also focused on influence of transient spark circuit configuration on HNO_2 formation.

We hypothesize that the enhanced NO production in transient spark generated by driving circuit with additional capacitor and inductor is attributable to the prolonged duration of the plasma, up to 4–5 μs, characterized by high gas temperature (up to 5000–7000 K) and a relatively high electron density of approximately 10^{21} m^{-3}. However, these prolonged, high-temperature conditions are likely detrimental to HNO_2 formation. The highest concentration of HNO_2 in humid N_2/NO mixture was obtained using circuit including only additional capacitor.

Spark current pulses are the strongest when using circuit with additional capacitor without inductor. One of the possible explanations for the most efficient formation of HNO_2 is based on more efficient formation of OH radicals. Alternatively, more efficient HNO_2 could be related to faster and more efficient turbulent mixing of the plasma channel containing the NO and OH radicals with the surrounding cold gas, which is beneficial for stabilizing HNO_2 molecules. Further research is needed to verify these hypothesis by laser induced fluorescence techniques, or by Schlieren imaging for visualization of gas dynamics.

The knowledge gained from this study will be used to further optimize the chemical effects of the transient spark. Within the microsecond timescale during which reactive plasma is sustained in the configuration with additional capacitor and inductor, we also anticipate a high vibrational temperature of molecules. Beyond nitrogen oxide formation, these conditions could also be suitable for carbon dioxide dissociation [58]. This represents another potential direction for our future research.

Acknowledgements Funded by the EU NextGenerationEU through the Recovery and Resilience Plan for Slovakia under the Project No. 09I03-03-V03-00033.

Data Availability Statement This manuscript has no associated data or the data will not be deposited. [Authors' comment: The data that support the findings of this study are available from the corresponding author upon reasonable request, or the raw data can be found at URL: http://enviro.fmph.uniba.sk/janda/data/ts-lc-oes2025.]

Declarations

Conflict of interest The authors have no conflicts to disclose.

Ethics statement Presented research does not include studies on human subjects, human data or tissue, or animals.

References

1. J.H. Urso, L.M. Gilbertson, Atom conversion efficiency: a new sustainability metric applied to nitrogen and phosphorus use in agriculture. ACS Sustain. Chem. Eng. **6**, 4453–4463 (2018). https://doi.org/10.1021/acssuschemeng.7b03600
2. J.W. Erisman, M.A. Sutton, J. Galloway, Z. Klimont, W. Winiwarter, How a century of ammonia synthesis changed the world. Nat. Geosci. **1**, 636–639 (2008). https://doi.org/10.1038/ngeo325
3. H. Liu, Ammonia synthesis catalyst 100 years: practice, enlightenment and challenge. Chin. J. Catal. **35**, 1619–1640 (2014). https://doi.org/10.1016/S1872-2067(14)60118-2
4. C. Smith, A.K. Hill, L. Torrente-Murciano, Current and future role of Haber-Bosch ammonia in a carbon-free energy landscape. Energy Environ. Sci. **13**, 331–344 (2020). https://doi.org/10.1039/C9EE02873K
5. B. Lin, F.H. Nowrin, J.J. Rosenthal, A.S. Bhown, M. Malmali, Perspective on intensification of Haber−Bosch to enable ammonia production under milder conditions. ACS Sustain. Chem. Eng. **11**, 9880–9899 (2023). https://doi.org/10.1021/acssuschemeng.2c06711
6. The future of food and agriculture: Drivers and triggers for transformation, 2022. . FAO (Food and Agriculture Organization of the United Nations). https://doi.org/10.4060/cc0959en
7. Y. Dellero, Manipulating amino acid metabolism to improve crop nitrogen use efficiency for a sustainable agriculture. Front. Plant Sci. **11**, 602548 (2020). https://doi.org/10.3389/fpls.2020.602548
8. S.V. The, R. Snyder, M. Tegeder, Targeting nitrogen metabolism and transport processes to improve plant nitrogen use efficiency. Front. Plant Sci. **11**, 628366 (2021). https://doi.org/10.3389/fpls.2020.628366
9. G.K. Hutchinson, L.X. Nguyen, Z. Rubio Ames, K. Nemali, R.S. Ferrarezi, Sensor-controlled fertigation management for higher yield and quality in greenhouse hydroponic strawberries. Front. Plant Sci. **15**, 1469434 (2025). https://doi.org/10.3389/fpls.2024.1469434
10. A. Soumare, A.G. Diedhiou, M. Thuita, M. Hafidi, Y. Ouhdouch, S. Gopalakrishnan, L. Kouisni, Exploiting biological nitrogen fixation: a route towards a sustainable agriculture. Plants **9**, 1011 (2020). https://doi.org/10.3390/plants9081011
11. N. Cherkasov, A.O. Ibhadon, P. Fitzpatrick, A review of the existing and alternative methods for greener nitrogen fixation. Chem. Eng. Process. Process Intensif.

90, 24–33 (2015). https://doi.org/10.1016/j.cep.2015.02.004
12. R.K. Raju, Electrocatalytic reduction of nitrogen to ammonia on metal nanoclusters: insights and trends from d- and p-block metals. Phys. Chem. Chem. Phys. **27**, 7773–7796 (2025). https://doi.org/10.1039/D5CP00046G
13. A. Fridman, *Plasma chemistry*, 1st edn. (Cambridge University Press, Cambridge, 2008). https://doi.org/10.1017/CBO9780511546075
14. Y. Gorbanev, E. Vervloessem, A. Nikiforov, A. Bogaerts, Nitrogen fixation with water vapor by nonequilibrium plasma: toward sustainable ammonia production. ACS Sustain. Chem. Eng. **8**, 2996–3004 (2020). https://doi.org/10.1021/acssuschemeng.9b07849
15. Z. Huang, A. Xiao, D. Liu, X. Lu, K (Ken). Ostrikov, Plasma-water-based nitrogen fixation: status, mechanisms, and opportunities. Plasma Process. Polym. **19**, 2100198 (2022). https://doi.org/10.1002/ppap.202100198
16. A. Klimek, D.G. Piercey, Nitrogen fixation via plasma-assisted processes: mechanisms, applications, and comparative analysis—a comprehensive review. Processes **12**, 786 (2024). https://doi.org/10.3390/pr12040786
17. D. Aceto, P.F. Ambrico, F. Esposito, Air cold plasmas as a new tool for nitrogen fixation in agriculture: underlying mechanisms and current experimental insights. Front. Phys. **12**, 1455481 (2024). https://doi.org/10.3389/fphy.2024.1455481
18. S. Ghavam, M. Vahdati, I.A.G. Wilson, P. Styring, Sustainable ammonia production processes. Front. Energy Res. **9**, 580808 (2021). https://doi.org/10.3389/fenrg.2021.580808
19. T. Kim, S. Song, J. Kim, R. Iwasaki, Formation of NOx from air and N2 /O2 mixtures using a nonthermal microwave plasma system. Jpn. J. Appl. Phys. **49**, 126201 (2010). https://doi.org/10.1143/JJAP.49.126201
20. M. Janda, V. Martišovitš, K. Hensel, Z. Machala, Generation of antimicrobial NOx by atmospheric air transient spark discharge. Plasma Chem. Plasma Process. **36**, 767–781 (2016). https://doi.org/10.1007/s11090-016-9694-5
21. E. Vervloessem, M. Aghaei, F. Jardali, N. Hafezkhiabani, A. Bogaerts, Plasma-based N2 fixation into NOx: insights from modeling toward optimum yields and energy costs in a gliding arc plasmatron. ACS Sustain. Chem. Eng. **8**, 9711–9720 (2020). https://doi.org/10.1021/acssuschemeng.0c01815
22. V.D. Rusanov, A.A. Fridman, G.V. Sholin, The physics of a chemically active plasma with nonequilibrium vibrational excitation of molecules. Sov. Phys. Usp. **24**, 447–474 (1981). https://doi.org/10.1070/PU1981v024n06ABEH004884
23. F. Zheng, K. Feng, S. Wu, W. Xiao, Experimental investigation into atmospheric microwave plasma-driven nitrogen fixation using metal-organic frameworks. Processes **12**, 2633 (2024). https://doi.org/10.3390/pr12122633
24. D. Trunec, Z. Navrátil, J. Tomeková, V. Mazánková, S. Ďurčányová, A. Zahoranová, Chemical composition of gaseous products generated by coplanar barrier discharge in air and N2/O2 mixtures. Plasma Sources Sci. Technol. **31**, 115011 (2022). https://doi.org/10.1088/1361-6595/ac9c8f
25. M. Janda, K. Hensel, Z. Machala, T.A. Field, The influence of electric circuit parameters on NOx generation by transient spark discharge. J. Phys. D Appl. Phys. **56**, 485202 (2023). https://doi.org/10.1088/1361-6463/ace634
26. I.A. Kossyi, A.Y. Kostinsky, A.A. Matveyev, V.P. Silakov, Kinetic scheme of the non-equilibrium discharge in nitrogen-oxygen mixtures. Plasma Sources Sci. Technol. **1**, 207–220 (1992). https://doi.org/10.1088/0963-0252/1/3/011
27. X. Fan, S. Kang, J. Li, T. Zhu, Formation of nitrogen oxides (N2O, NO, and NO2) in typical plasma and plasma-catalytic processes for air pollution control. Water Air Soil Pollut. **229**, 351 (2018). https://doi.org/10.1007/s11270-018-4011-y
28. Z. Wang, M. Zhu, D. Liu, L. Liu, X. Wang, J. Chen, L. Guo, Y. Liu, M. Hou, M. Rong, N2 O5 in air discharge plasma: energy-efficient production, maintenance factors and sterilization effects. J. Phys. D Appl. Phys. **56**, 075204 (2023). https://doi.org/10.1088/1361-6463/acb65f
29. B. Wenjuan, Y. Xiangli, Nitrogen fixation into HNO3 and HNO2 by pulsed high voltage discharge. Plasma Sci. Technol. **9**, 288–291 (2007). https://doi.org/10.1088/1009-0630/9/3/08
30. M. Janda, K. Hensel, P. Tóth, M.E. Hassan, Z. Machala, The role of HNO2 in the generation of plasma-activated water by air transient spark discharge. Appl. Sci. (Basel) (2021). https://doi.org/10.3390/app11157053
31. F. Rezaei, P. Vanraes, A. Nikiforov, R. Morent, N. De Geyter, Applications of plasma-liquid systems: a review. Materials **12**, 2751 (2019). https://doi.org/10.3390/ma12172751
32. R. Zhou, R. Zhou, P. Wang, Y. Xian, A. Mai-Prochnow, X. Lu, P.J. Cullen, K (Ken). Ostrikov, K. Bazaka, Plasma-activated water: generation, origin of reactive species and biological applications. J. Phys. D Appl. Phys. **53**, 303001 (2020). https://doi.org/10.1088/1361-6463/ab81cf
33. P. Bruggeman, C. Leys, Non-thermal plasmas in and in contact with liquids. J. Phys. D Appl. Phys. **42**, 053001 (2009). https://doi.org/10.1088/0022-3727/42/5/053001
34. F. Bilea, M. Garcia-Vaquero, M. Magureanu, I. Mihaila, V. Mildažienė, M. Mozetič, J. Pawłat, G. Primc, N. Puač, E. Robert, A. Stancampiano, I. Topala, R. Žūkienė, Non-thermal plasma as environmentally-friendly technology for agriculture: a review and roadmap. Crit. Rev. Plant Sci. **43**, 428–486 (2024). https://doi.org/10.1080/07352689.2024.2410145
35. C. Bradu, K. Kutasi, M. Magureanu, N. Puač, S. Živković, Reactive nitrogen species in plasma-activated water: generation, chemistry and application in agriculture. J. Phys. D Appl. Phys. **53**, 223001 (2020). https://doi.org/10.1088/1361-6463/ab795a
36. N.K. Kaushik, B. Ghimire, Y. Li, M. Adhikari, M. Veerana, N. Kaushik, N. Jha, B. Adhikari, S.-J. Lee, K. Masur, T. Von Woedtke, K.-D. Weltmann, E.H. Choi, Biological and medical applications of plasma-activated

media, water and solutions. Biol. Chem. **400**, 39–62 (2018). https://doi.org/10.1515/hsz-2018-0226

37. Z. Machala, B. Tarabová, D. Sersenová, M. Janda, K. Hensel, Chemical and antibacterial effects of plasma activated water: correlation with gaseous and aqueous reactive oxygen and nitrogen species, plasma sources and air flow conditions. J. Phys. D Appl. Phys. **52**, 034002 (2019). https://doi.org/10.1088/1361-6463/aae807
38. M.J. Pavlovich, D.S. Clark, D.B. Graves, Quantification of air plasma chemistry for surface disinfection. Plasma Sources Sci. Technol. **23**, 065036 (2014). https://doi.org/10.1088/0963-0252/23/6/065036
39. L. Nani, F. Tampieri, E. Ceriani, E. Marotta, C. Paradisi, ROS production and removal of the herbicide metolachlor by air non-thermal plasma produced by DBD, DC− and DC+ discharges implemented within the same reactor. J. Phys. D Appl. Phys. **51**, 274002 (2018). https://doi.org/10.1088/1361-6463/aab8b9
40. Z. Wang, X. Wang, S. Xu, R. Zhou, M. Zhang, W. Li, Z. Zhang, L. Wang, J. Chen, J. Zhang, L. Guo, D. Pei, D. Liu, M. Rong, Off-site production of plasma-activated water for efficient disinfection: the crucial role of high valence NOx and new chemical pathways. Water Res. **267**, 122541 (2024). https://doi.org/10.1016/j.watres.2024.122541
41. M. Janda, V. Martišovitš, Z. Machala, Transient spark: a dc-driven repetitively pulsed discharge and its control by electric circuit parameters. Plasma Sources Sci. Technol. **20**, 035015 (2011). https://doi.org/10.1088/0963-0252/20/3/035015
42. M. Janda, Z. Machala, A. Niklová, V. Martišovitš, The streamer-to-spark transition in a transient spark: a dc-driven nanosecond-pulsed discharge in atmospheric air. Plasma Sources Sci. Technol. **21**, 045006 (2012). https://doi.org/10.1088/0963-0252/21/4/045006
43. P. Pareek, S. Kooshki, P. Tóth, M. Janda, Tuning composition of plasma activated water generated by transient spark discharge with electrospray. Chem. Eng. J. **493**, 152583 (2024). https://doi.org/10.1016/j.cej.2024.152583
44. N. Konjević, A. Lesage, J.R. Fuhr, W.L. Wiese, Experimental Stark Widths and Shifts for Spectral Lines of Neutral and Ionized Atoms (A Critical Review of Selected Data for the Period 1989 Through 2000). J. Phys. Chem. Ref. Data **31**, 819–927 (2002). https://doi.org/10.1063/1.1486456
45. A. Lesage, Experimental Stark widths and shifts for spectral lines of neutral and ionized atoms a critical review of selected data for the period 2001–2007. New Astron. Rev. **52**, 471–535 (2009). https://doi.org/10.1016/j.newar.2008.01.001
46. M.A. Gigosos, M.Á. González, V. Cardeñoso, Computer simulated Balmer-alpha, -beta and -gamma Stark line profiles for non-equilibrium plasmas diagnostics. Spectrochim. Acta B, At. Spectrosc. **58**, 1489–1504 (2003). https://doi.org/10.1016/S0584-8547(03)00097-1
47. H.-J. Kunze, *Introduction to plasma spectroscopy. Springer series on atomic, optical, and plasma physics* (Springer, Berlin, 2009)
48. C.O. Laux, Radiation and nonequilibrium collisional-radiative models, von Karman Institute Lecture Series 2002–07, Physico-Chemical Modeling of High Enthalpy and Plasma Flows, eds. D. Fletcher, J.-M. Charbonnier, G.S.R. Sarma, and T. Magin, Rhode-Saint-Genèse, Belgium (2002)
49. Specair (2007) http://www.specair-radiation.net
50. C.O. Laux, T.G. Spence, C.H. Kruger, R.N. Zare, Optical diagnostics of atmospheric pressure air plasmas. Plasma Sources Sci. Technol. **12**, 125–138 (2003). https://doi.org/10.1088/0963-0252/12/2/301

51. U. Fantz, Basics of plasma spectroscopy. Plasma Sources Sci. Technol. **15**, S137–S147 (2006). https://doi.org/10.1088/0963-0252/15/4/S01
52. M. Janda, T. Hoder, A. Sarani, R. Brandenburg, Z. Machala, Cross-correlation spectroscopy study of the transient spark discharge in atmospheric pressure air. Plasma Sources Sci. Technol. **26**, 055010 (2017). https://doi.org/10.1088/1361-6595/aa642a
53. T. Hoder, Z. Bonaventura, A. Bourdon, M. Šimek, Sub-nanosecond delays of light emitted by streamer in atmospheric pressure air: analysis of N2(C3Πu) and N2+(B2Σu+) emissions and fundamental streamer structure. J. Appl. Phys. **117**, 073302 (2015). https://doi.org/10.1063/1.4913215
54. F. Bastien, E. Marode, Stark broadening of Hα and Hβ in ionized gases with space-charge field. J. Quant. Spectrosc. Radiat. Transf. **17**, 453–469 (1977). https://doi.org/10.1016/0022-4073(77)90093-0
55. M. Janda, V. Martišovitš, K. Hensel, L. Dvonč, Z. Machala, Measurement of the electron density in transient spark discharge. Plasma Sources Sci. Technol. (2014). https://doi.org/10.1088/0963-0252/23/6/065016
56. G.V. Naidis, Simulation of streamer-induced pulsed discharges in atmospheric-pressure air. Eur. Phys. J. Appl. Phys. **47**, 22803 (2009). https://doi.org/10.1051/epjap/2009084
57. N.G. Bykova, A.L. Kusov, G.Y. Gerasimov, I.E. Zabelinskii, P.V. Kozlov, VYu. Levashov, Effect of absorption on the broadening of spectral lines and the radiation intensity of shock-heated air. Fluid Dyn. **59**, 1437–1451 (2024). https://doi.org/10.1134/S0015462824604261
58. A. Bogaerts, G. Centi. Plasma technology for CO_2 conversion: a personal perspective on prospects and gaps. Front. Energy Res.**8**, 111. (2020). https://doi.org/10.3389/fenrg.2020.00111